Quantum-Effect Devices

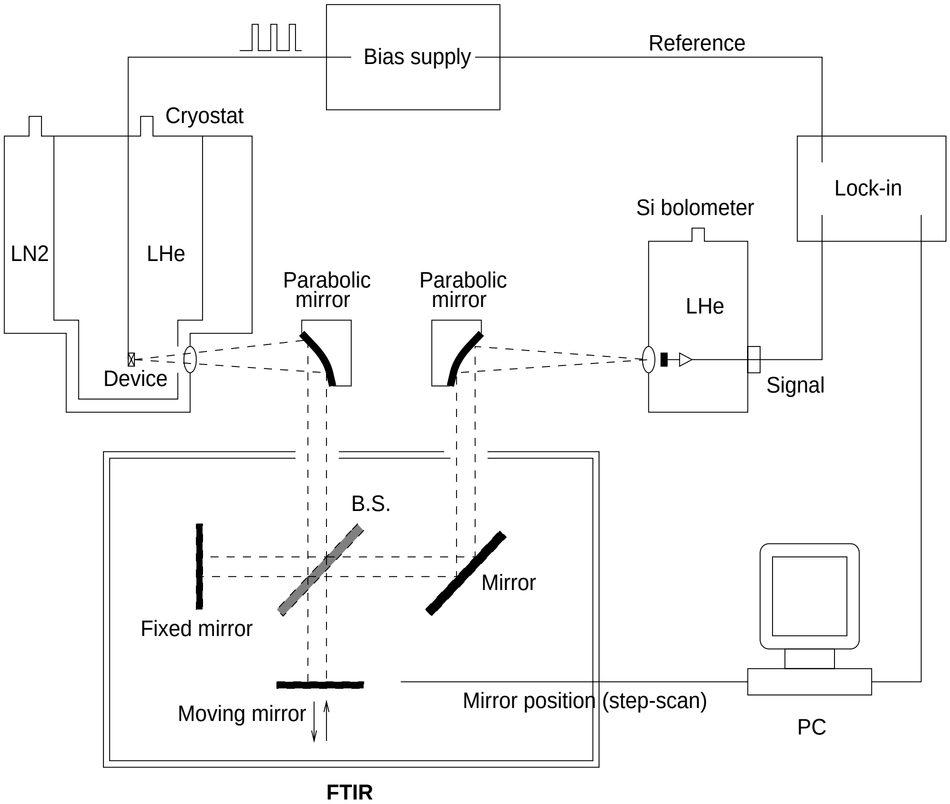

Far-infrared measurement set-up that uses an external Fourier transform spectrometer to spectrally resolve the emitted THz signals.
Courtesy: B. Xu, B. Williams, and Q. Hu, and M. Melloch at Purdue University

Quantum-Effect Devices

- *Optically pumped THz emitters using quantum wells*
- *Intersubband-transition lasers*
  Electrically pumped THz emitters using quantum wells
- *Millimeter-wave, Terahertz, and Infrared Devices*
- *Mid-infrared quantum-cascade lasers*
- *Picosecond Time-Resolved Transport Studies of Quantum-Effect Devices*
- *A Superconducting Vortex Qubit*
- *Triangular Arrays of Josephson Junctions*
- *Nonlinear Dynamics Of Discrete Josephson Arrays*
- *Meissner-like states in Josephson Arrays*
- *Engineering Josephson Oscillators*
- *Discrete Breathers in Josephson Arrays*
- *Coupled Rings of Josephson Junctions: Interactions of Topological Kinks*

Optically pumped THz emitters using quantum wells

Personnel

I. Lyubomirsky (Q. Hu in collaboration with M. R. Melloch, Purdue University)

Sponsorship

AASERT through U.S. Army Research Office, Hertz Foundation Fellowship

Compared to electrical pumping, optical pumping offers advantages of an easier design, a higher selectivity in pumping, and a separation of the pump and electrical bias. For THz emitters, easily available CO_2 lasers can be used as the pumping source. We first designed a three-level system for THz emission. However, this structure showed an excessive heating when it is pumped by an intense CO_2 laser. In order to increase the emission efficiency and therefore the gain of the active medium, we have redesigned our optically pumped THz emitters based on a four-level system using coupled triple quantum wells, as shown in Fig. 1. Electrons on the ground state E_1 can be pumped by a CO_2 laser to the E_4 level. By carefully engineering the scattering rates between subband levels by choosing subband energy separations and spatial locations, a population inversion between E_3 and E_2 can be achieved. It was estimated that a modal gain of approximately 100 cm^{-1} can be achieved at a 1-W average pump power level. Recently, we have observed spontaneous intersubband emission from a 4-level system pumped by a CO_2 laser.

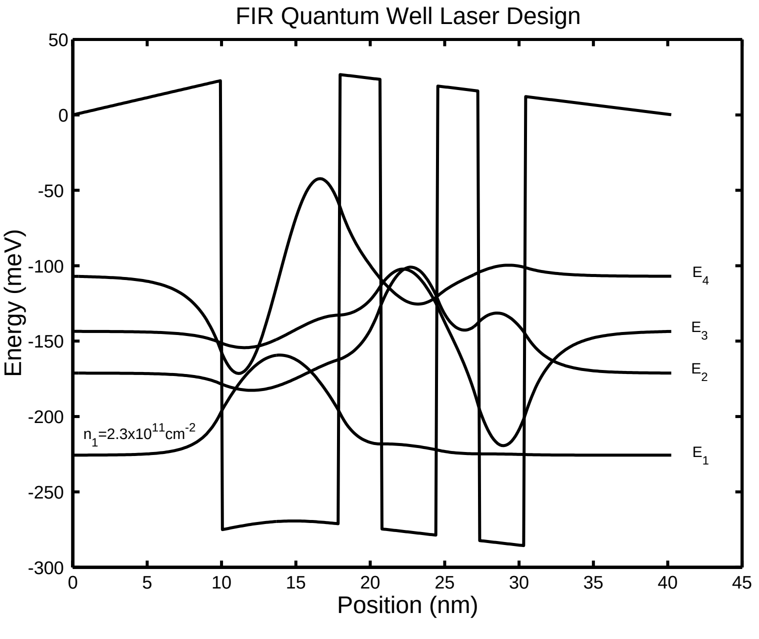

Fig. 1: Schematic of a four-level system based on a coupled triple quantum-well structure. Electrons can be pumped from the E_1 to the E_4 level by a CO_2 laser. They then quickly relax to the E_3 level by LO-phonon scattering. Similarly, the electrons on the E_2 level can be emptied quickly to E_1 through LO-phonon scattering. THz emission is to take place between E_3 and E_2.

Intersubband-transition lasers
Electrically pumped THz emitters using quantum wells

Sponsorship

U.S. Army Research Office

Personnel

B. Xu, B. Williams, and Q. Hu, in collaboration with M. Melloch at Purdue University

Semiconductor quantum wells are human-made quantum mechanical systems in which the energy levels can be designed and engineered to be of any value. Consequently, unipolar lasers based on intersubband transitions (electrons that make lasing transitions between subband levels within the conduction band) were proposed for long-wavelength sources as early as the 1970s. However, because of the great challenge in epitaxial material growth and the unfavorable fast nonradiative relaxation rate, unipolar intersubband-transition lasers (also called quantum-cascade lasers) at near-infrared (4-5 micron) and mid-infrared (8-11 micron) wavelengths were developed only recently at Bell Laboratories. This achievement is remarkable, but the technique used in the original quantum-cascade lasers will not be directly applicable for the longer-wavelength THz range because of two major obstacles. First, the energy levels corresponding to THz frequencies (1 THz = 4 meV) are quite narrow, so the requirements for the design and fabrication of suitable quantum wells are demanding. Because of the narrow separation between subband levels, heating and hot-electron tunneling will have a much greater effect. Also, the small energy scales of THz photons make the detection and analysis of spontaneous emission (a crucial step toward developing lasers) quite difficult. Second and perhaps the most important, mode confinement, which is essential for any laser oscillation, is difficult at longer wavelengths. Conventional dielectric-waveguide confinement is not applicable because the evanescent field penetration, which is proportional to the wavelength and is on the order of several tens of microns, is much greater than the active gain medium of several microns. We are currently developing intersubband-transition lasers based on our recent success in generating and detecting THz emission signals and on a novel mode confinement method using metallic waveguide structures.

Our MQW structure for THz emission is shown in Figure 2, in which the conduction band profile and the square of the wave functions were calculated self-consistently from Schrödinger and Poisson equations. The device is formed by a triple-well structure using GaAs/$Al_{0.3}Ga_{0.7}As$ materials, as shown in the dashed box. This structure is essentially a three-level system (marked as E_3, E_2, and E_1 in Figure 2; the level E_4 is much higher in energy so it does not contribute to transport at low biases), which is required for any lasers. Because there is no recombination involved in unipolar intersubband lasers, electrons can be "reused" many times. Consequently, many identical triple-well modules can be cascade-connected,

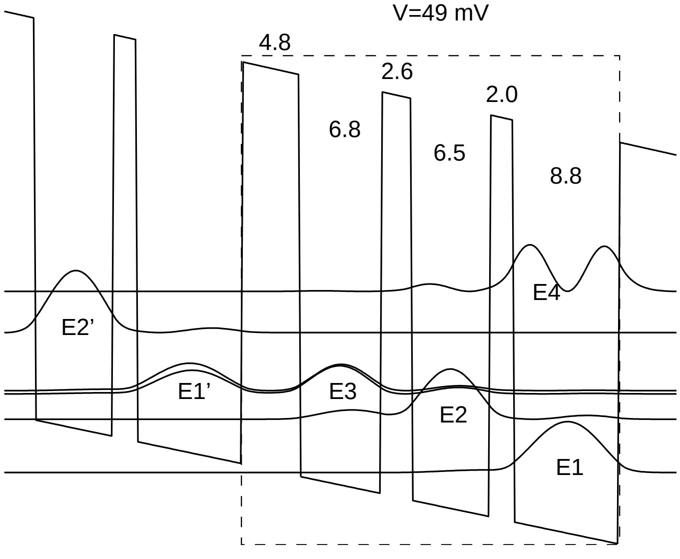

Fig. 2: Schematic of a three-level system based on a triple quantum-well structure. The radiation transition takes place between E_3 and E_2, and the fast LO-phonon emission keeps the level E_2 empty. The conduction-band

continued

continued

and the emission power and the mode confinement factor can be increased substantially. Due to translational symmetry, design analysis needs to focus only on one module, provided there are no global space charges and high-field domains. The collector barrier (the one with a 2.0-nm thickness) is center _-doped at approximately $10^{11}/\mathrm{cm}^2$ in order to provide dynamic charges to assure a global charge neutrality. The radiative transition takes place between E_3 and E_2, with an energy separation of $\Delta E_{32} \approx 14$ meV and an oscillator strength of $f_{32} \approx 0.31$ (using the effective mass in GaAs). Under the designed bias of 50 mV per module, the ground state E_1' of a previous module is aligned with E_3. Thus, the upper subband E_3 can be selectively populated through resonant tunneling. The energy separation between E_2 and E_1 was designed to be 36 meV under the bias, which corresponds to the LO-phonon energy Ó$_{-LO}$ in GaAs. Once energetically allowed, the very fast LO-phonon scattering (with a time $_{-21} \approx 1.4$ ps) will rapidly depopulate the E_2 level and establish a population inversion between E_3 and E_2.

The MQW structures were grown in the Molecular-Beam Epitaxy (MBE) machine in the group of our collaborator Professor M. R. Melloch at Purdue University. In order to verify the accuracy of our design calculations and to inspect the quality of quantum wells and interfaces, we performed an infrared absorption measurement with the

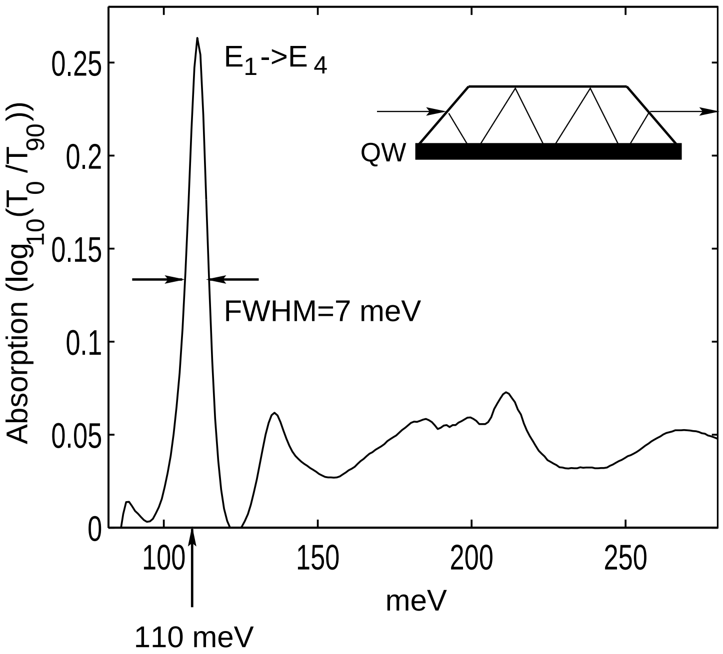

Fig. 3: Infrared absorption measurement of a 80-module device, which was placed at room temperature. The absorption peak is due to the E_1_E_4 intersubband transition. The measured FWHM is 7 meV, including a 4-meV instrumental linewidth. The measured intersubband transition frequency (110 meV) and dipole moment (14 Å) agreed quite well with the calculated values of 109 meV and 12 Å.

continued

continued

result shown in Figure 3. The measurement was performed on a 80-module device (with a total of 240 quantum wells) at room temperature. A mid-infrared absorption peak is clearly seen at 110 meV, which is due to the intersubband transition from E_1 to E_4. The FWHM is only 7 meV, including a 4-meV instrumental linewidth. This narrow linewidth is an indication of the high quality and uniformity of the wells and interfaces. Furthermore, the measured E_1_E_4 transition frequency of 110 meV and the dipole moment of 14 Å (deduced from the area of the absorption peak) agreed quite well with the calculated values of 109 meV and 12 Å, indicating the accuracy of our calculations.

In order to measure the intersubband THz emission and resolve its spectra, we constructed a set-up that included an external Fourier Transform Infrared Spectrometer (FTIR) with a composite Si bolometer as its detector. The system's schematic is shown in Figure 4. We have improved this system and perfected our measurement techniques so that THz emission measurements can be routinely performed on our emitters with output power levels of 1-10 pW.

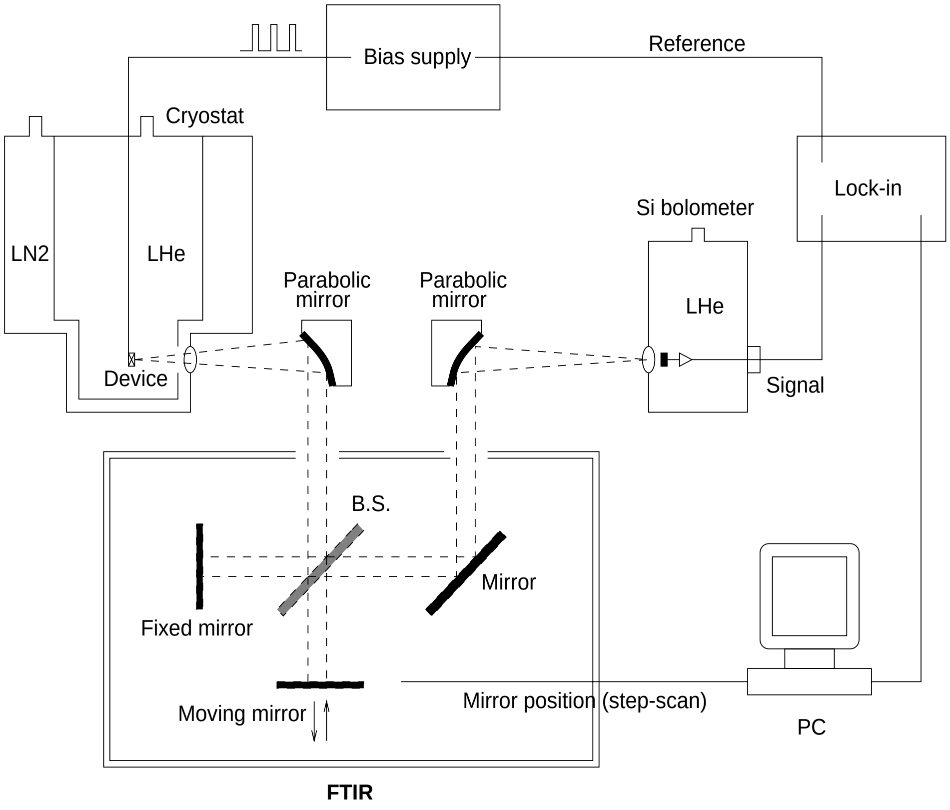

Fig. 4: Far-infrared measurement set-up that uses an external Fourier transform spectrometer to spectrally resolve the emitted THz signals.

Millimeter-wave, Terahertz, and Infrared Devices

Personnel

E. Duerr, K. Konistis, I. Lyubomirsky, B. Riely, B. Williams, B. Xu, N. Zamdmer, and
G. de Lange (Qing Hu)

Sponsorship

Not Provided

Millimeter-wave and THz frequencies (f > 100 GHz) remain one of the most underdeveloped frequency ranges, even though the potential applications in remote sensing, spectroscopy, plasma diagnostics, and communications are obviously great. This is because the millimeter wave and far-infrared frequency range falls between two other frequency ranges in which conventional semiconductor devices are usually operated. One is the microwave frequency range, and the other is the near-infrared and optical frequency range. Semiconductor devices which utilize the classical diffusive transport of electrons, such as diodes and transistors, have a high frequency limit. This limit is set by the transient time and parasitic RC time constants. Currently, electron mobility and the smallest feature size which can be fabricated by lithography limit the frequency range to below several hundred GHz. Semiconductor devices based on quantum mechanical interband transitions, however, are limited to frequencies higher than those corresponding to the semiconductor energy gap, which is higher than 10 THz for most bulk semiconductors. Therefore, a large gap exists from 100 GHz to 10 THz in which very few devices are available.

Semiconductor quantum-effect devices (which can be loosely termed “artificial atoms”), including both vertically grown quantum-well structures and laterally confined mesoscopic devices, are human-made quantum mechanical systems in which the energy levels can be chosen by changing the sizes of the devices. Typically, the frequency corresponding to the intersubband transitions is in the millimeter-wave range (DE ~ 1-4 meV) for the lateral quantum-effective devices, and THz to infrared for the vertical quantum wells. It is therefore appealing to develop ultrahigh-frequency devices, such as radiation detectors and mixers, and THz and infrared lasers utilizing the intersubband transitions in these devices.

In addition to new physical concepts, novel technologies must also be developed to meet the challenges at these high frequencies. Conventional mechanically machined horn antennas integrated with waveguide cavities have been the work horse at microwave and millimeter-wave frequencies since they were first implemented more than fifty years ago during World War II. Very high antenna gain and essentially perfect antenna efficiency can be achieved using these structures. However, they are expensive, bulky, and incompatible with arrays. In order to overcome these problems, new development has been made to use micromachining to fabricate the horn antenna structures. In these structures, the active elements and their planar antennas are fabricated on a free-standing thin (~1 micron) SiN membrane, which is suspended over a silicon pyramidal horn that is formed by anisotropic etching, or micromachining. The side walls of this micromachined structure can then be coated with Au to form a horn antenna. Compared to conventional waveguide horn antennas, this novel micromachined structure has several major advantages. It is easier to fabricate fine three-dimensional structures by using photolithography. Horn antennas with micron precision can be easily defined and inexpensively mass produced. It is made on Si or GaAs wafers and compatible with thin-film technology. Thus, active elements, such as RF and IF amplifiers, mixers and video detectors, local oscillators, and post-detection signal processors, can be integrated monolithically with the antenna structures to form monolithic transmitter/receiver systems. It is light-weight and compact. The most attractive feature of the micromachined structure is that focal-plane arrays can be fabricated easily on a single wafer, as illustrated in Figure (Next Page). Such systems will yield a significantly improved spatial resolution in remote sensing, and a much greater antenna gain when implemented with phased-arrays.

continued

continued

In our group, we are systematically investigating physical and engineering issues that are relevant to devices operating from millimeter-wave to infrared frequencies. Specifically, we are working on micromachined millimeter-wave focal-plane arrays, and development of terahertz and infrared lasers based on intersubband transitions.

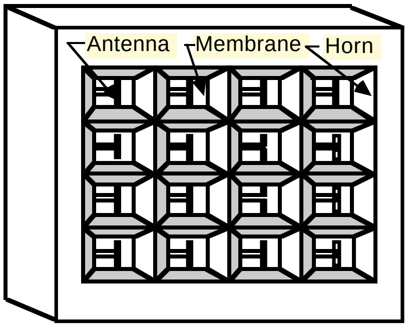

Mid-infrared quantum-cascade lasers

Personnel

B. Williams, B. Riely, and Q. Hu, in collaboration with M. R. Melloch at Purdue University.

Sponsorship

Army Research Laboratory Federated Lab.

High-power, compact mid-infrared (8-12 micron) lasers are very useful tools for remote sensing, end-point detection in dry etching processes, point-to-point communication, and night vision applications. Conventional laser diodes operating in this long wavelength range use narrow-gap lead-salt semiconductors, which require cryogenic operations, provide relatively low power levels, and have very limited frequency tunability. Recently developed Quantum-Cascade (QC) lasers based on intersubband transitions have shown much higher operating temperatures and a great frequency tunability. These features make them ideal for the above-mentioned applications. In this project, we are developing mid-infrared quantum-cascade lasers based on GaAs/AlGaAs quantum-well structures. Compared to the InGaAs/InAlAs materials used in the original quantum-cascade lasers developed at Bell Labs, the GaAs/AlGaAs system offers a much higher thermal conductivity (approximately a factor of 20 compared to InGaAs/InAlAs) and therefore a higher-power operation.

The core of our MQW structure is a tightly coupled double quantum well, in which three energy levels form the three-level lasing structure. These energy levels are shown in Fig. 8. The lasing transition is to take place between E_3 and E_2, with the energy separation approximately 120 meV, corresponding to 10-micron wavelength. The energy separation between E_2 and E_1 is designed to be approximately 36 meV, which is the energy of LO phonon in GaAs. Consequently, the energy level E_2 will be depopulated by very fast LO-phonon scattering (~0.2 ps). Our design of the MQW structures is aided by a numerical code that solves Shrödinger and Poisson equations self-consistently, and it includes the effect of band nonparabolicity to account for the much higher energy levels corresponding to infrared frequencies.

continued

continued

The superlattice structure sandwiching the active region serves the purpose of selective injection of electrons into the E_3 level, and selective removal of electrons from both E_2 and E_1 levels. By choosing the period of the superlattice properly, the Bragg reflection results in minigaps (transport forbidden) and minibands (transport allowed), as shown in both Figures 5 and 6. The combination of the selective injection into E_3 and the fast removal from E_2 will assure an inverted population between these two levels. We calculated the dipole moment for the $E_3\_E_2$ transition to be approximately 23 Å, which yields a modal gain of 480 cm^{-1} for a doping concentration of $1.5\_10^{11}/\text{cm}^2$. Such a high level of gain is characteristic of the QC lasers in which the two subbands track each other in momentum, resulting in a large joint density of states.

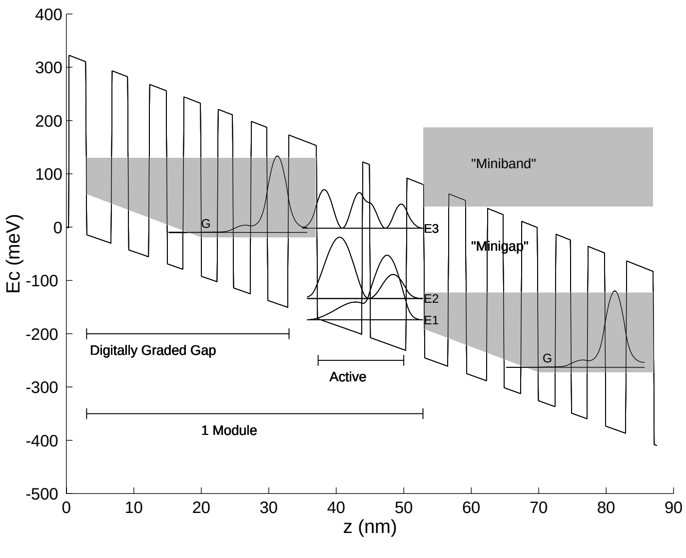

Fig. 5: Conduction-band profile and wave functions of the designed MQW structure that contains a three-level gain medium and superlattices for selective injection and removal of electrons.

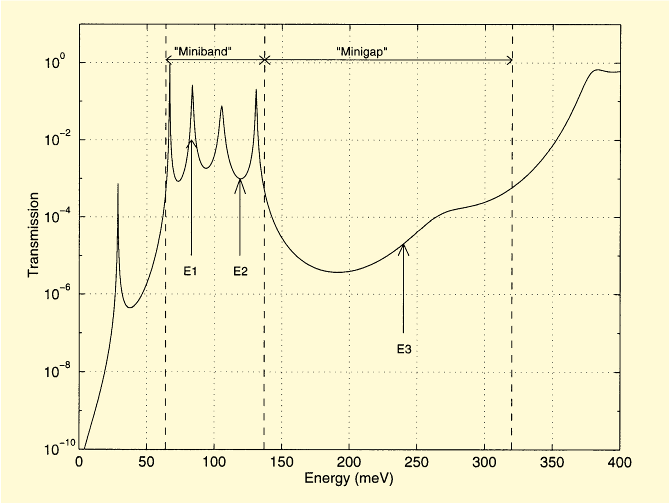

Fig. 6: Calculated transmission coefficient of the superlattice sandwiching the core structure. The valley in the transmission corresponds to the minigap and the peaks form the miniband.

continued

continued

We have fabricated a MQW structure consisting 40 nominally identical structures as shown in Figure 5. We have performed emission measurements using the FTIR system shown in Figure 7. An emission spectrum with the narrowest linewidth is shown in Figure 7. The center frequency of 121 meV (corresponding to 10-micron wavelength) is what we designed for, and the FWHM linewidth is only 10.8 meV. This linewidth is comparable to the narrowest achieved at Bell Labs using InGaAs/InAlAs structures, and is an indication of the high interface quality and uniformity of our MQW structures. Currently, we are designing suitable cladding layers for mode confinement to achieve lasing.

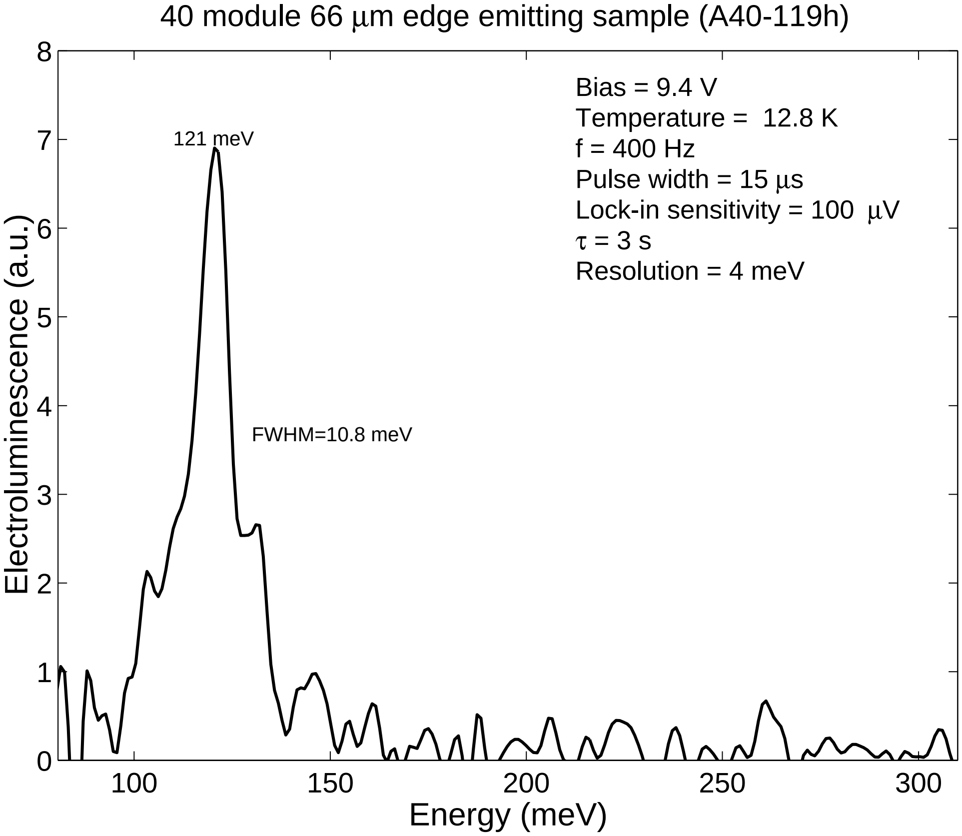

Fig. 7: Spectrum of spontaneous intersubband emission from a 40-module MQW structure whose design is shown in Fig. 8.

Picosecond Time-Resolved Transport Studies of Quantum-Effect Devices

Personnel

N. Zamdmer and Q. Hu

Sponsorship

NSF/MRSEC

Our previous work in frequency domain has yielded new information about quantum-effect devices, a complementary approach is to study the response of the quantum devices in time-resolved fashion by using a pump-and-probe method with a pulsed laser. A 100-fs laser pulse contains frequency components up to 10 THz, which should enable us to perform spectroscopic studies on quantum devices over a broad frequency range that covers all the interesting energy levels, namely the intersubband transition and Coulomb interaction energies. Furthermore (and perhaps the most attractive feature of the time-domain studies), the time-resolved studies can reveal information that frequency-domain studies cannot reveal, namely the time scale of transport process in quantum devices. This is one of the basic issues in determining the potential applications of the quantum devices.

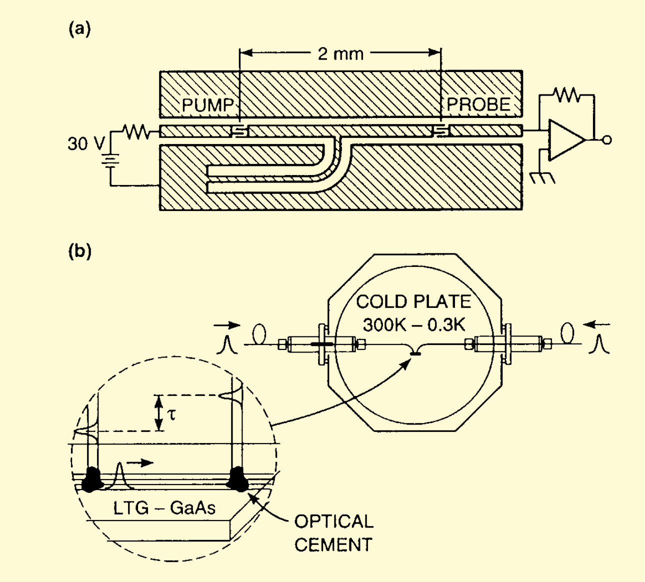

Fig. 8: (a) Two Austin switches coupled through a coplanar transmission line.
(b) Schematic of a cryostat with optical fiber couplers that bring subpicosecond laser pulses to the cryogenic stage.

In order to pursue the time-resolved pump-and-probe measurements on quantum-effect devices, we have constructed a cryostat with optical fiber couplers that can bring sub-picosecond laser pulses to the cryogenic stage. The schematic of the system is shown in Figure 8, along with the schematic of coplanar transmission lines that provide the dc biases of the pump and probe Austin switches and the propagation path for the generated picosecond electrical pulses.

Our initial successful testing of the cryogenic pump-and-probe system was performed using the coupling structure shown in Figure 8. In this structure, two Auston switches are coupled through a co-planar transmission line without any disruptions. This is the simplest coupling scheme to implement, and it provides an efficient propagation of the picosecond pulses with minimal attenuation and distortion. However, such a simple structure does not allow an easy insertion of a three-terminal device in between the pump and probe switches. In order to insert a three-terminal device, the ground planes surrounding the center conductor must be broken to allow two electrical contacts to the center conductor, which will be the source (on the side of the pump switch) and drain (on the side of the probe switch). Such broken ground planes will cause a significant distortion and attenuation on the propagating pulses, making the measurement results difficult to interpret.

continued

continued

In order to overcome this difficult technical problem, we have developed a novel coplanar waveguide circuit whose schematic is shown in Figure 9. In this structure, the two isolated ground planes in the center can serve as two separate gate electrodes. The ground plane on the left can serve as the contact to the source, and the ground plane on the right can serve as the contact to the drain. Furthermore, each Auston switch has two separate dc biases. This way, if the optical illumination to the pump and probe switches is misaligned (which is unavoidable especially in a fiber-coupled cryogenic environment), the generated photocurrent can be compensated by the two biases, and a pure TEM mode can be generated and detected. Our preliminary measurements on this structure yielded encouraging results, showing the separate dc biases can largely compensate misaligned optical pulses.

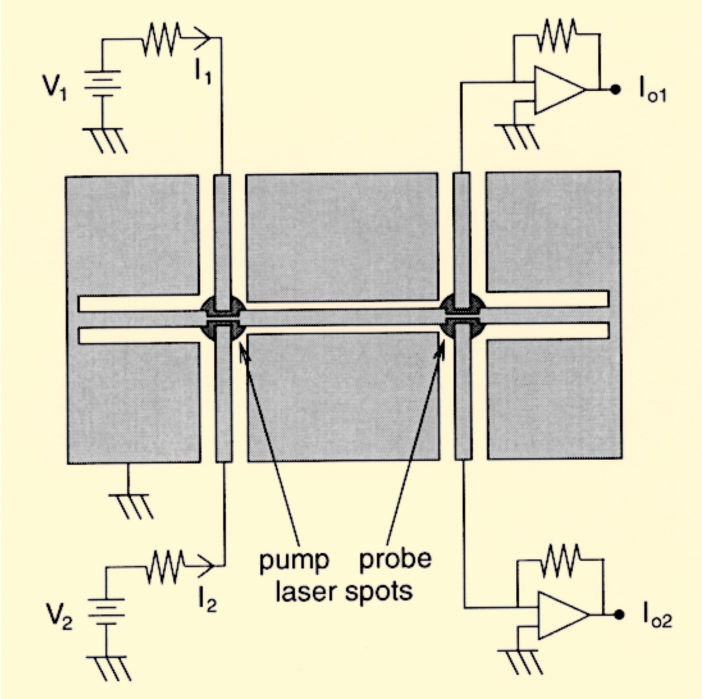

Fig. 9: A novel coplanar waveguide structure that provides an easy integration with a three-terminal device and a compensation of misaligned optical pulses.

A Superconducting Vortex Qubit

Personnel

L. Tian, D. S. Crankshaw, C. H. van der Wal, J. J. Mazo (L. Levitov, S. Lloyd, and J. E. Mooij (Delft University of Technology, The Netherlands), T. P. Orlando

Sponsorship

ARO

Quantum computers are devices that store information on quantum variables such as spins, photons, and atoms, and that process that information by making those variables interact in a way that preserves quantum coherence. Typically, these variables consist of two-state quantum systems called quantum bits or 'qubits'. To perform a quantum computation, one must be able to prepare qubits in a desired initial state, coherently manipulate superpositions of a qubit's two states, couple qubits together, measure their state, and keep them relatively free from interactions that induce noise and decoherence.

We have designed a superconducting qubit that has circulating currents of opposite sign as its two states. The circuit consists of three nano-scale aluminum Josephson junctions connected in a superconducting loop and controlled by magnetic fields as shown in Figure 10.

Each junction is marked by an "x" and is modeled by a parallel combination of an ideal Josephson junction and a capacitor C_i. The parallel resistive channel is assumed negligible. The ideal Josephson junction has a current-phase relation, $I_i=I_c\sin\varphi_i$ where φ_i is the gauge-invariant phase of junction *i*.

Quantum calculations of the energy levels and induced currents in this system have been performed. This system can be mapped onto a two state quantum system, similiar in form to NMR, with an equivalent Hamiltonian of the form

$$H = E_0\,\sigma_z + \delta_1\,\sigma_x$$

where δ_1 is proportional to the oscillating fields. These systems are estimated to work in the GHz regime and to have decoherence times of the order of milliseconds. Furthermore, the calculations show that the quantum states obey all five functional requirements for a quantum bit:

(1) The superconducting circuit is at sufficiently a low temperature that the vortex qubits can easily be prepared in their ground state.
(2) The vortex states can be manipulated precisely with magnetic fields.
(3) Two vortex qubits can be readily coupled inductively.
(4) The flux of the vortex states can be detected and measured using a SQUID-type detector.
(5) In contrast with charge quantum states in Josephson circuits, the vortex states can be made insensitive to background charges and effectively decoupled from their electrostatic environment. The magnetic coupling to the vortex states and the environment can also be made sufficiently weak.

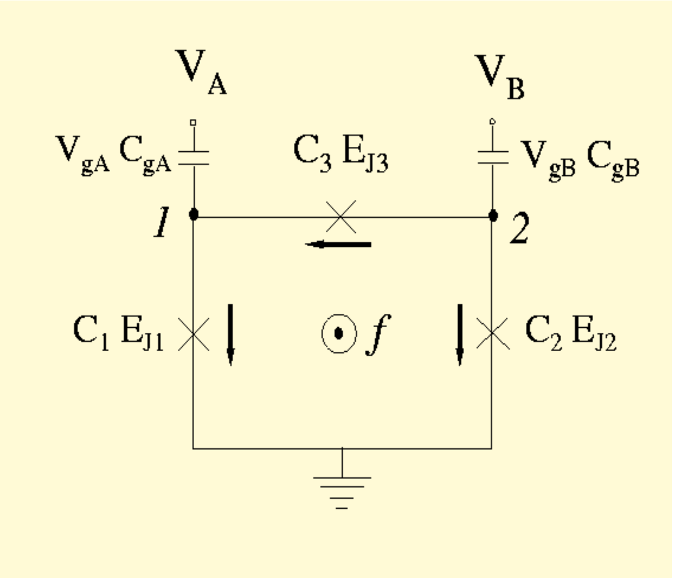

Fig. 10: The three-junction qubit. Josephson junctions 1 and 2 both have Josephson energies E_J and capacitance C and Josephson junction3 has a Josephson energy and capacitance α times smaller. The nodes 1 and 2 represent the superconducting islands (nodes) which are coupled by gate capacitors $C_g= \gamma C$ to gate voltages V_A and V_B. The arrows define the direction of the currents. The flux is taken out of the page.

Triangular Arrays of Josephson Junctions

Personnel

A.E. Duwel, P. Caputo (KFA, Julich, GE), A. Ustinov (Universität Erlangen- Nüremberg, GE), S. Yukon and N.C. H. Lin (Rome Air Force Laboratory, Rome, New York) (T. P. Orlando)

Sponsorship

AFOSR, Rome Air Force Laboratory

Triangular arrays of Josephson junctions operating in an applied magnetic field have been proposed as a way of obtaining useful power levels of mm and sub-mm wave radiation generated by the AC Josephson effect. A triangular one-dimensional (1D) array consists of a single row of parallel biased triangular cells which have a Josephson junction in each branch (Figure 11). The bias current is uniformly applied through resistors at each point indicated by arrows in the sketch, and the array voltage response is read across the row. In order to characterize high frequency properties, the horizontal junctions of the array (x-direction) are integrated in an insulating SiO$_2$ layer of a superconducting microstripline ending with a finline antenna. The antenna transforms the array impedance into the waveguide impedance through two exponentially tapered Nb fins.

In the presence of a field, two resonances appear on the IV curve, corresponding to L_sC and L_JC resonances. These steps are characteristics of single cells, and their voltage does not change with the number of cells in the array. At the L_sC resonance, triangular arrays produce large-amplitude single-harmonic oscillations in the horizontal junctions. High frequency measurements of a 12 cell triangular array reveal the presence of radiation emitted from the transverse junctions. Figure 12 shows the radiated power P_{rad} at 75 GHz, detected at the L_sC step. The radiation frequency is proportional to the step voltage. Measurements of longer rows will be taken to test the scaling of power with the number of horizontal junctions.

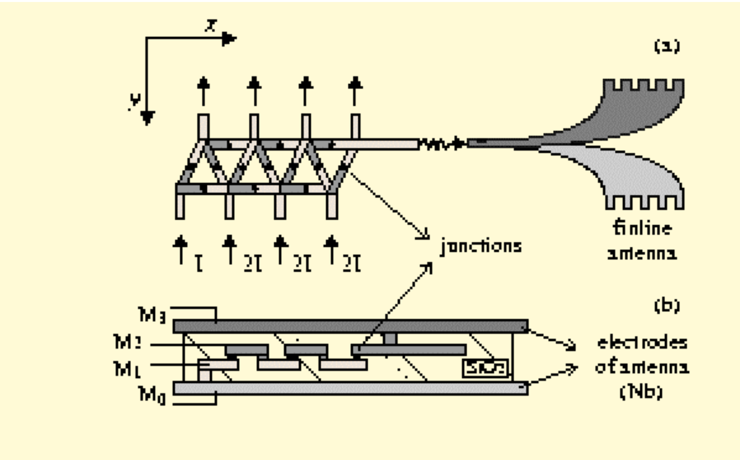

Fig. 11: Schematic top view of a 6 cell triangular array with the finline antenna which couples the array signal to the 80-120 GHz rectangular waveguide (a) and a cross view of the horizontal junctions of the array inserted in the microstripline ending into the antenna (b).

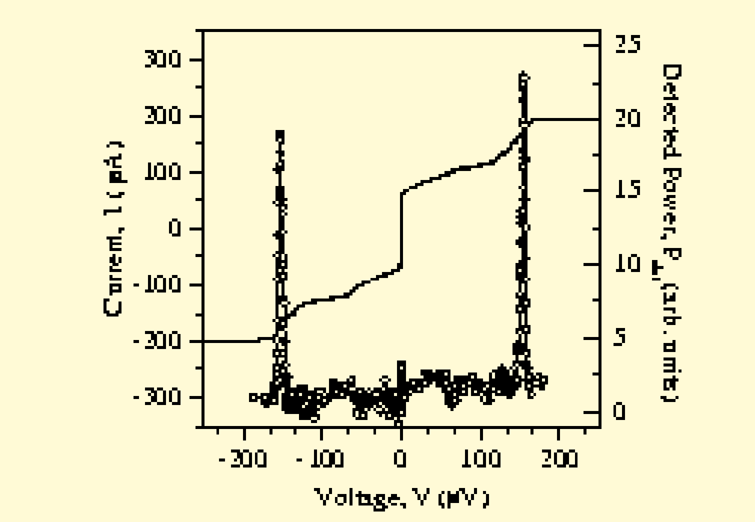

Fig 12: Measurement of radiation emission from a 12 cell array. The IV curve is shown together with the detected radiation power at a frequency of 75 GHz. The detector bandwidth is 0.9 GHz.

Nonlinear Dynamics Of Discrete Josephson Arrays

Personnel

E. Trías, M. Barahona (Stanford University, Palo Alto, California), A. E. Duwel, Dr. H. S. J. van der Zant (Delft University of Technology, The Netherlands), S. Watanabe (Ibaraki University, Japan), and S. H. Strogatz (Cornell University, Ithaca, New York) (T. P. Orlando)

Sponsorship

NSF

Discrete arrays of nonlinear Josephson oscillators can exhibit diverse spatiotemporal patterns. Although such oscillator arrays are difficult to analyze completely, one can often use the symmetries of the system to construct simple patterns composed of spatially repeated "unit cells". Experiments, simulations, and analysis on a broad class of discrete arrays of Josephson-junction oscillators indicate novel phase-locked states that due to their special symmetry reduce the governing equations of the full array to a much smaller set of equations of a unit cell. Networks ranging from single square and triangular plaquettes to one- and two-dimensional arrays have been studied.

Figure 13 shows the measured *IV* curves (*I* is the current per vertical junction normalized by I_c, and *V* is the voltage per row) for three different array geometries when fully frustrated. The signature of all these *IV*s is the appearance of jumps at two resonant voltages, V_+ and V_-. The upper step, which ends at V_+ is independent of temperature suggesting that local geometrical properties determine the voltage. In this state, all the rows of the array act coherently and phase-lock at a voltage that depends on the geometric loop inductance and junction capacitance. The lower voltage *V*-, on the other hand, is temperature-dependent, suggesting a dependence on the Josephson inductance and the geometric loop inductance. By taking advantage of the symmetry of the network it is possible to describe the solution as a dynamical checkerboard state and mathematically analyze its resonant behavior in a reduced system of governing equations. However, the conditions for the stability and the temporal periodicity of the checkerboard state, and the dynamics associated with other possible states, are challenging problems for future investigation.

We have also studied the spatiotemporal dynamics of circular one-dimensional arrays of underdamped Josephson junctions connected in parallel. In these Josephson rings, a traveling wave solution consisting of a single kink can be trapped and studied experimentally without the complications caused by reflections off boundaries. We find that a propagating kink can become phase-locked to linear waves excited in its wake.

In the *IV* curve, resonant steps are observed indicative of this phase-locking. Resonant steps also occur in the *IV* curves for higher voltages in the return path of the subgap region. These resonant steps have a completely different origin and occur at voltages where the periodic whirling solution undergoes an instability parametrically amplified by the linear modes in the system.

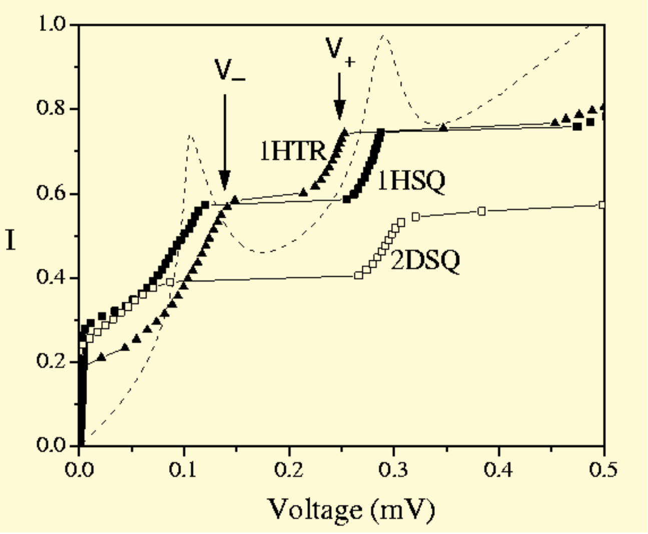

Figure 13: Experimental IV curves for three arrays: triangular array (1 x 9 plaquettes) with $\beta_c = 8$ *and* $\lambda = 0.64$; *square array (1 x 7) with* $\beta_c = 11$ *and* $\lambda = 0.76$; *and a square array (7 x 7) with* $\beta_c = 20$ *and* $\lambda = 0.92$. *Dashed line, IV from harmonic balance for the squarer array (1 x 7) array with the same* β_c *and an effective* $\lambda_{eff} = 0.61$ *which accounts for mutual inductance effects.* V_+ *and* V_- *are indicated.*

Meissner-like states in Josephson Arrays

Personnel

E. Trías and J. K. Jensen (T. P. Orlando)

Sponsorship

NSF

One of the most striking features of superconducting materials is their ability to expel an applied flux. This perfect diamagnetism is direct expression of macroscopic quantum mechanical effects and is usually called the Meissner effect. A Meissner state occurs when the induced flux caused by persistent currents in the superconducting material almost perfectly cancels the applied flux.

In order to study this effect in Josephson networks, we designed several ladder arrays with different number of rows. The arrays consist of square loops with junctions on both vertical and horizontal edges. As we increase the applied current from zero, the array is superconducting and therefore has zero output voltage. At some critical current the array develops a finite voltage and the zero voltage state is destroyed. It is in this zero voltage state that the Meissner state can exist.

To measure the critical current of an array, we first apply a perpendicular magnetic field, H_A. Once the field is set, the current is swept from zero until the output voltage reaches a threshold value that is typically set to 1μV. Figure 14 shows representative I_{dep} vs. applied field curves for four different arrays: 47 x 47, 3 x 47, 2 x 47, and 1 x 15. The 47 and 15 refer to the number cells in the direction normal to current injection while the smaller number is the number of rows in the direction of the applied current.

We find generic features for all the measurements regardless of temperature or array topology. First, the shape of the I_{dep} curves is periodic with the applied field. We normalize the applied field so that $f = H_A / H_{period}$ and the curves become periodic with $f = 1$. Secondly, the curves are almost symmetric about $f = 0.5$. The details of the I_{dep} vs. f curves are sample dependent as shown in Fig. 9. For the 47 x 47 ladder, we find that a large narrow peak is observed at $f = 0$. As f is increased the curve quickly decays to an average level of 0.17. There are smaller peaks that are evident at $f = 1/4$, $f = 1/3$ and $f = 1/2$. The 3 x 47 array has a similar features to the fully two-dimensional system. The peak at $f = 0$ is now broader as marked by the arrow. The decay to the average level is linear but the substructure appears at different f values. When the array only has two rows we see curves typical to the 2 x 47 ladder. The $f = 0$ peak is now very broad, but the decay is still linear. All of the other structure has disappeared except for the $f = 0.5$ peak. Finally, when we measure an array with only one row, the $f = 0$ peak has expanded so that even the $f = 0.5$ substructure has disappeared. It is this peak at $f = 0$ that can be described as a Meissner-like state.

After performing numerical simulations to characterize the Josephson network dynamics, we have developed a model that reproduces the experimental characteristics. We find that even if the geometrical inductances are neglected, the Josephson junctions that circumvent the network can act as parametric inductors that support a circulating current. As the network becomes more two-dimensional it becomes increasingly difficult to support the large circulating current and so the Meissner-like state narrows. The linear decay can be described in terms of Ampère's law. However, it is still not fully understood how the state is destroyed nor what the substructure that is so evident in Figure 14 represents. We will continue to investigate these and other unsolved problems.

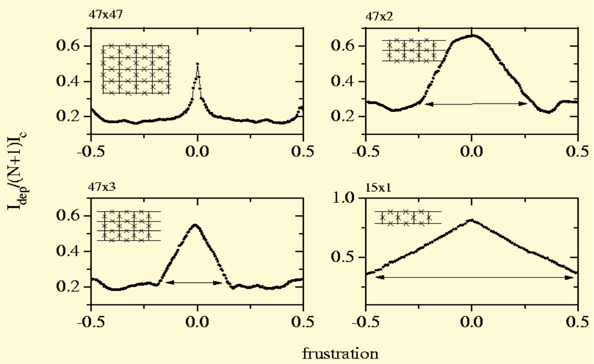

Fig. 14: I vs. frustration for four different arrays: 47 x 47, 3 x 47, 2 x 47, and 1 x 15. The 47 and 15 refers to the number cells in the direction normal to current injection while the smaller number is the number of rows in the direction of the applied current. Lines with arrows indicate broadening of $f = 0$ peak as the number of rows of the array decreases.

Engineering Josephson Oscillators

Personnel

E. Trías, A. E. Duwel, D. S. Crankshaw, and Prof. S. Watanabe (Ibaraki University, Japan) (T. P. Orlando)

Sponsorship

NSF

As the telecommunications revolution pushes for denser utilization of the spectrum, there is a need to develop inexpensive sources and detectors that operate in the 100\thinspace GHz to several THz range. It is precisely in this range that Josephson junctions provide an almost ideal solid state, current controllable source.

Arrays of junctions provide for relatively large power but due to non-linearities they can exhibit diverse complex spatiotemporal patterns. Experiments, simulations and analysis were performed on a broad range of discrete arrays of Josephson-junction oscillators in order to understand their ability to produce coherent radiation. Networks ranging from single square and triangular plaquettes to one- and two-dimensional arrays are studied. In each array, the junctions are identical and underdamped, and the arrays are driven by dc bias currents. Although few analytical results are known for these systems, we study the technically interesting solutions which can be represented as traveling waves. It is in this mode that the devices can be used as submillimeter wave sources.

Using the mathematical technique of harmonic balance it is possible to create an equivalent linear circuit of a Josephson network that is operating in a traveling wave mode. Though the non-linearity of the system allows for mixing of all the harmonics, in underdamped systems we find that the first harmonic is orders of magnitude stronger than the rest. In general any variable can be decomposed in terms of its dc and ac spectrum. If we further restrict the ac component to a single frequency as suggested by our simulations, then the branch current and voltage across a junction can be written as

$$I = I_{DC} + i_{ac} e^{j\omega t}$$
$$V = V_{DC} + v_{ac} e^{j\omega t}$$

Our equivalent circuit then consists of a dc bias circuit and a mixing circuit that creates the first harmonic. Figure 15 depicts the equivalent circuit. Here k

$$I_c = e^{j\,k}$$

$$I_M = \frac{v_{ac}}{j\omega} \frac{e^{-jk}}{2}$$

represents the phase difference between the first harmonic and the rotating part of the Josephson oscillation, and the mixing current, I_M, represents the nonlinear interaction between them. This equivalent circuit makes it possible to use powerful circuit theoretic tools to understand a Josephson network.

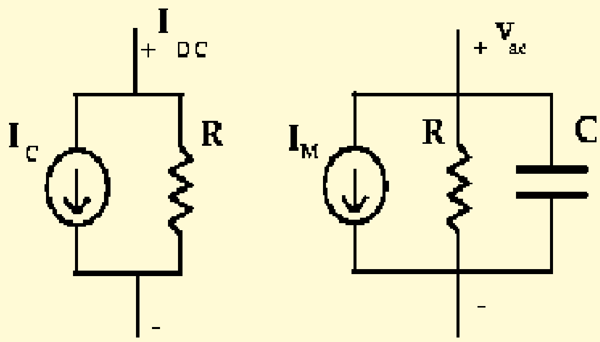

Fig. 15: Equivalent circuit for a Josephson junction in a voltage state and with a single harmonic. Non-linearity is captured by I_M which is a mixing current that describes the interaction between the rotating Josephson phase and its first harmonic.

A natural application of the circuit model is the study of the effect that the boundaries have on the traveling wave. Figure 16 shows the spatial distribution of first harmonic amplitudes in a parallel Josephson array of 54 junctions. The graph (a) shows the array with open boundaries. In general the shape will depend on the array parameters, but at this value of applied field the spatial part of the solution is symmetric. The reflection of the traveling wave is clearly evident on both the entry and exit sides of the array. Using the above circuit model it is possible to determine a load impedance that will minimize the reflection. Graph (b) shows the result when the impedance matching load is applied to junction one. The reflection at the left hand boundary is reduced substantially.

We plan to use the linear circuit model to understand how to optimize a Josephson oscillator design so that a minimum of linewidth is obtained while providing a maximum of power and frequency tunability.

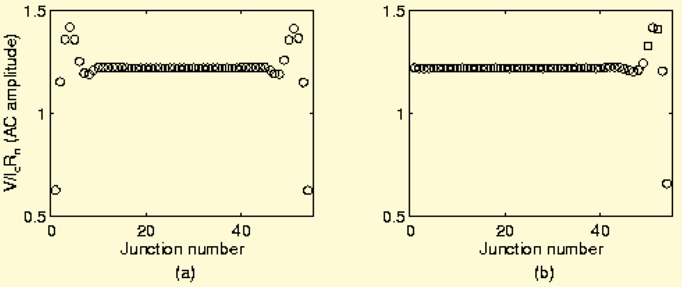

Fig. 16: Amplitudes of first harmonics of vertical junctions in a parallel array.
Graph (a) is an array with open boundaries while
(b) shows the same array with a matching load at junction one.

Discrete Breathers in Josephson Arrays

Personnel

J. J. Mazo and E. Trías (T. P. Orlando)

Sponsorship

NSF, Fulbright/MEC Fellowship

Linear models of crystals have been instrumental in developing a physical understanding of the solid state. Thermodynamic properties such as specific heat, transport properties such as electron relaxation times or superconductivity, and interactions with radiation can be understood by modeling a crystal as a lattice of atoms with fixed harmonic interactions. This leads to the conventional phonon-like analysis with a basis of plane wave normal modes. However certain properties of solids, such as thermal expansions, cannot be understood in this model. For example, the elastic constants of the atomic interactions may depend on the temperature or the volume and so make the interaction non-linear. This is termed an anharmonic effect and the usual approach is to use a more generalized Taylor expansion for the lattice interaction that includes more than just the harmonic term.

Until quite recently anharmonic effects were studied as perturbations to the fully solvable harmonic model. Then it was discovered that the non-linearity may lead to localized vibrations in the lattice that cannot be analyzed using the standard plane wave approach. These intrinsic localized modes have been termed discrete breathers because their amplitudes oscillate around a few sites in the lattice and they do not depend on impurities for their localization. Because discrete breathers have been proven to be generic modes in many non-linear lattices, they have been the object of great theoretical and numerical attention. However, they have yet to be generated and detected in an experiment.

We have designed experiments to detect a localized mode in Josephson-junction anisotropic ladder arrays biased by dc external currents. For this, we have done numerical simulations of the dynamics of an open ladder including induced fields at experimentally accessible values of the parameters of the array. We have developed a method for exciting a breather in the array. We distinguish between two families of solutions which

continued

continued

present different voltage patterns in the array. Both types are robust to random fluctuations and exist over a range of parameters values and array sizes.

Our anisotropic ladders (see Figure 17) contain junctions of two different critical currents: I_{ch} for the horizontal junctions and I_{cv} for the vertical ones. The anisotropy parameter h can then be defined as $h = I_{ch}/I_{cv}$. The horizontal junctions act as the coupling term between the vertical junctions and, due the sinusoidal current phase dependence of the junction, the interactions of the vertical junctions are anharmonic with h serving as the measure of interaction strength. Figure 17 shows schematically simple localized modes. The arrows indicate junctions that are rotating. All the other junctions librate at their equilibrium points. Type A breathers [see Figure 17 (a)], are characterized by one vertical and two horizontal rotating junctions. The second family, breather B [Figure 17 (b)], is characterized by one vertical and four horizontal rotating junctions.

Since a rotating junction outputs a dc voltage, the breather solutions can easily be detected by measuring the average voltage of the different vertical and horizontal junctions.

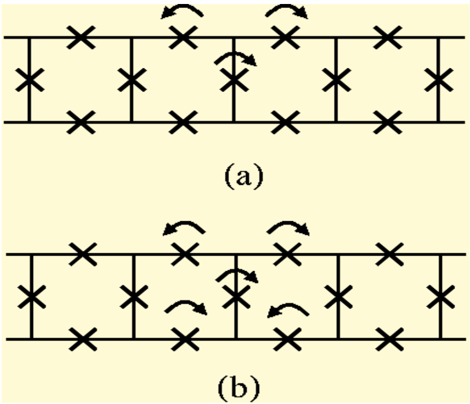

Fig. 17: Schematic picture of breather solutions in ladder array: type A (a) and type B (b) breathers. Arrows are associated with rotating junctions.

Type A and type B breathers exist close to the $h = 0$ limit. We then calculate the maximum value of the anisotropy for which the breather exists as a stable solution of the dynamical equations for different values of the normalized cell inductance λ. Figure 18 shows the result. We start with a type B breather and $h \sim 0.001$. As we increase h, type B solutions become unstable and the solution evolves to a type A breather. As we further increase h this breather becomes unstable and the system usually jumps to either a pinned or a whirling state. To verify that our procedures are accurate, we have calculated Floquet multipliers for periodic breather solutions and found results consistent with those shown in the Figure 18.

Using the above results, appropriate Josephson arrays have been fabricated and will be measured to test the various properties of discrete breather excitations. Just as the discovery of soliton solutions led to the deeper understanding of non-linear systems and subsequent application to many fields outside the solid state community, it is hoped that the study of discrete breathers will add a new mathematical tool with which to unlock further mysteries of complex non-linear systems.

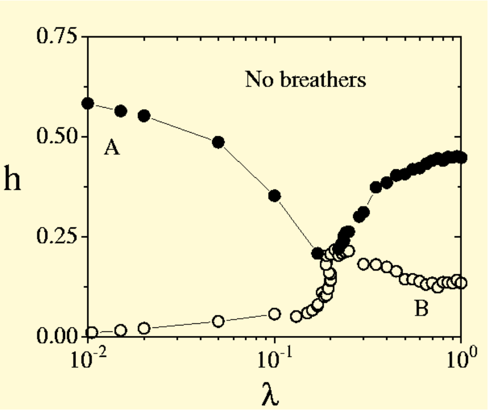

Fig. 18: Maximum values of anisotropy for the existence of typeA (solid circles) and type B (open circles) breather solutions at different values of λ in an 8 cell ladder. Lines serve as a guide to the eyes.

Coupled Rings of Josephson Junctions: Interactions of Topological Kinks

Personnel

A. E. Duwel, P. Heij, E. Trías, Dr. H. S.J. van der Zant (Delft University of Technology, The Netherlands), and Prof. S. H. Strogatz (Cornell University, Ithaca, New York) (T. P. Orlando)

Sponsorship

NSF

We explore a system of two discrete rings of underdamped oscillators, using inductively coupled Josephson junctions as an experimental realization. This Josephson system is a model system for studying spatiotemporal dynamics of coupled oscillators, and more specifically for exploring kink interactions in discrete lattices, a topic that is also important in, e.*g*., the dynamics of dislocations and ferromagnetic domain walls.

The layout of a discrete coupled ring system with N junctions per ring is shown in Figure 19 for $N = 4$. The Nb - AlO_x - Nb junctions are 3 x 3 μm^2, and the radius of the outer ring is 28 μm. When the system is cooled in the presence of a perpendicular magnetic field to below the superconducting transition, the total flux bounded by the continuous superconducting rings becomes trapped in units of $\phi_o = h/2e$. A single unit of quantized flux is called a vortex if the flux is along the applied field and an anti-vortex if it is opposite. A vortex and anti-vortex correspond to a kink and anti-kink. If there are $m_{v,in}$ and $m_{v,out}$ kinks in the two rings, and $m_{v,in}$ and $m_{a,out}$ anti-kinks, then the net, conserved phase winding in each ring is $M_{in} = m_{a,in} - m_{a,in}$ and $M_{out} = m_{v,out} - m_{a,out}$.

In Figure 19 we show a simulated IV characteristic for the case of $M_{in} = 1$ and $M_{out} = 0$. There are $N = 51$ junctions in each ring. For a range of bias currents ($I_b < 0.57\ I_c$), kink/anti-kink pairs are excited in the outer ring. In the figure, we use an open circle to represent kinks and a cross to represent the anti-kink. The inset shows the relative motions of the kinks and the anti-kink when one pair is excited in the outer ring. As the bias current is applied, the kinks and anti-kink begin to rotate, producing a dc voltage across each ring.

In Figure 20, we plot the average dc voltage for each ring vs. bias current. As the current is increased, the kinks move faster, and the dc voltage increases. The kinks and anti-kinks phase-lock with linear waves, and, at certain speeds, further increases in the bias current tend to increase the amplitudes of the excited linear waves rather than the speed of a kink. As a result, at a step of almost constant voltage appears in the IV. These special speeds are given by the dispersion relation for linear waves in the coupled system, which is split into two branches. We refer to the inner ring step at 0.0151 I_cR_n as an Eck step, since the single trapped kink is near its maximum speed and no additional pairs are excited. When pairs are excited, their contributions simply add up (to lowest order), resulting in voltage steps at much larger voltages. We refer to these as High-Voltage (HV)

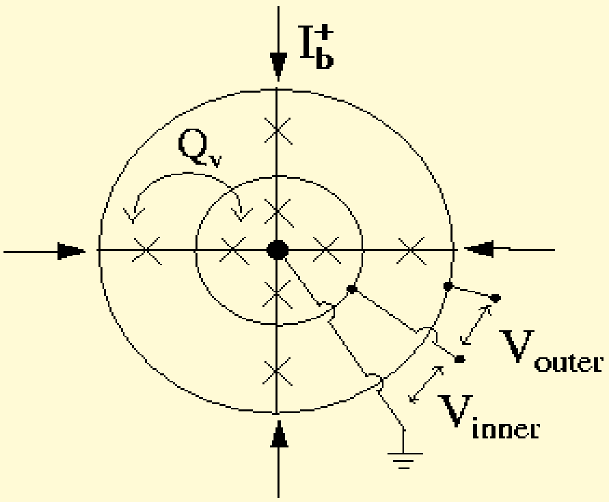

Fig. 19: Schematic of inductively coupled ring system. A uniform current Ib is fed into each node, as indicated by arrows and is extracted from the center island. In experiments, we measure the dc voltages V_{inner} *and* V_{outer}. Q_v *is the mutual inductance between two adjacent cells of the inner and outer rings.*

continued

continued

steps, since they are similar to states that can exist on the return path of an isolated ring. A study of the particular dynamics on these steps reveals that the coupling between the rings gives rise to phase-locking between kinks of the same sign in different rings. The kinks in both rings travel together at the same speeds. The anti-kinks travel in an opposite direction and can even have speeds which are different from the kinks.

In experiments of $N = 4$ and $N = 8$ systems, we discovered another interaction effect. For every distinct combination of $M_{in} \neq M_{out}$, we observe a parameter regime where pairs are excited only in the outer ring, another parameter regime where pairs are excited only in the inner ring, and a transition region in temperature from one state to the other. In addition, in several experiments we observe a very narrow range of temperature where there is a time-dependent competition between the two states. Based on the time scales of the fluctuations, the dynamics are likely to be influenced by weak noise in the input parameters. However, the sudden vulnerability of the system at this particular point also implies the presence of an instability and the possibility of a novel dynamical state. Future experiments will address the role of noise in this two-state competition.

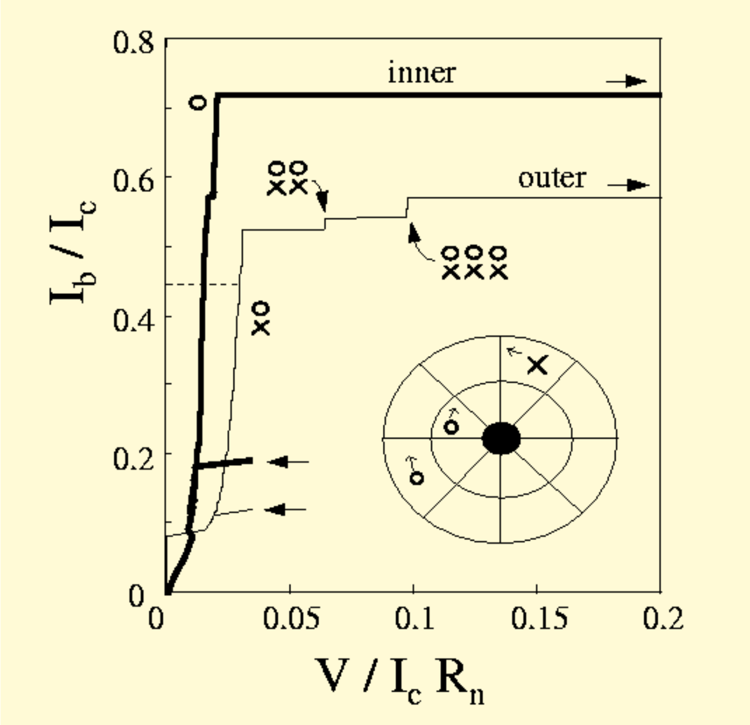

Fig. 20: Simulated IV characteristic. The nearly constant voltage steps correspond to the motion of the kinks (represented by open circles) and anti-kinks (represented by crosses) at their maximum speeds. The inset shows the relative motion of the kinks and the anti-kink for one excited pair in the outer ring.